Fe-incorporated TiO_2 nanotube arrays: Electronic structure and magnetic response

Pegah M. Hosseinpour,[1,*] Félix Jiménez-Villacorta,[1,†] Jing Liu,[1,2,‡] Badih A. Assaf,[3,§] Ian J. McDonald,[1,4] Dario Arena,[2,¶] Don Heiman,[3] Latika Menon,[3] and Laura H. Lewis[1,5,**]

[1]*Department of Chemical Engineering, Northeastern University, Boston, Massachusetts 02115*
[2]*National Synchrotron Light Source, Brookhaven National Laboratory, Upton, New York 11973*
[3]*Department of Physics, Northeastern University, Boston, Massachusetts 02115*
[4]*Department of Electrical and Computer Engineering, Northeastern University, Boston, Massachusetts 02115*
[5]*Mechanical and Industrial Engineering Department, Northeastern University, Boston, Massachusetts 02115*

(Received 11 May 2018; published 30 November 2018)

Incorporating Fe atoms into the lattice is shown to significantly alter electronic and magnetic properties of TiO_2 nanotubes synthesized by electrochemical anodization of Ti-Fe alloy sheets. The effects of Fe incorporation on the nanotube morphology, crystallinity, crystal structure, magnetic behavior and electronic structure were investigated with crystallographic and magnetic probes, including synchrotron-based spectroscopy. Results indicate that the iron cations predominately adopt the Fe^{3+} configuration, leading to a large increase of the electronic density of states at the Fermi energy. This increase is anticipated to provide enhanced catalytic action, for instance, in the degradation of water and of air pollutants. These results provide insight for tailoring the functionality of these nanostructures for energy-related applications.

DOI: 10.1103/PhysRevB.98.195145

I. INTRODUCTION

TiO_2 nanotube arrays with small amounts of iron (1–2 at. %) are semiconductors with versatile multifunctionality [1] appropriate for a plethora of potential applications, including as photocatalysts [2,3], sensors and solar cells [4,5], and perhaps as new kinds of oxide-based dilute magnetic semiconductors for spin-electronic applications [6,7]. As the functions underlying these potential applications are determined by the electronic structure, it is paramount to elucidate interrelations between the crystal structure, band structure, and the magnetic response. While studies of Fe-incorporated TiO_2 nanotube arrays synthesized by anodization of Ti-Fe alloys have shown an enhanced absorption of solar irradiation [8–10], analyses of correlations between the electronic, crystalline, and magnetic properties in these ordered nanostructures is deficient in detail [11,12].

In this study, the element-specific electronic structure of Ti(Fe)O_2 nanotube arrays is correlated with bulk magnetic properties as influenced by the degree of crystallinity and by the chemical composition (i.e., concentration of Fe). Ordered arrays of amorphous Fe-incorporated TiO_2 nanotubes (Fe cationic concentration of 2 at. %) were synthesized via electrochemical anodization from a Ti-Fe (∼4 at. % Fe) precursor alloy and annealed in an oxygen atmosphere to form the anatase structure. Connections between the morphology, crystal structure, and magnetic properties of the pure (i.e., Fe-free) and the Fe-incorporated nanotubes were investigated in both the as-synthesized and annealed states. The anatase structure of the Fe-incorporated nanotubes possesses an expanded unit cell and a higher degree of crystallinity relative to that obtained without Fe and is confirmed by magnetometry to be in a Fe^{+3} oxidation state. The magnetic moment of Fe-incorporated nanotubes is attributed to the Fe^{3+} ions. Results from this study provide fundamental knowledge for tailoring the TiO_2-based nanostructures, with an extension to the other oxide-based semiconductors, for an enhanced functionality in a variety of applications.

*Present address: Saint-Gobain Performance Plastics, Taunton, Massachusetts 02780; hossienpour.p@gmail.com.
†Present address: Consorcio ESS-Bilbao. Parque Tecnológico Bizkaia. Poligono Ugaldeguren III, Pol. A, 7B. 48170 Zamudio, Spain.
‡Present address: Department of Physics, Manhattan College, Riverdale, New York 10471.
§Present address: Département de Physique, Ecole Normale Supérieure, PSL Research University, CNRS, 24 rue Lhomond, 75005 Paris, France.
¶Present address: Department of Physics, University of South Florida, Tampa, Florida 33620.
**Author to whom correspondence should be addressed: lhlewis@neu.edu

II. EXPERIMENTAL BACKGROUND

A. Synthesis and processing of TiO_2 nanotubes

The pure and Fe-incorporated nanotube arrays were synthesized by electrochemical anodization of a $25 \times 25 \times 1\ mm^3$ Ti-Fe sheet (∼4 at. % Fe) that was formed by vacuum arc-melting of Fe and Ti and subsequently cold-rolled. A platinum mesh was used as the cathode and the anodization electrolyte consisted of ethylene glycol (98%, Sigma-Aldrich), potassium fluoride (0.05 M) and 1 vol. % deionized water. The duration of the anodization was approximately 4 h under an applied voltage of 60 V_{DC}. A titanium foil (99.97% pure, 127 μm-thick, Sigma-Aldrich) of similar dimensions

was anodized in the same conditions as described, to yield nominally pure nanotubes.

After anodization, the nanotube arrays were rinsed with 99.9% pure isopropyl alcohol and dried under a gentle airflow. Unsupported nanotube arrays (free-standing flakes) were obtained by mechanically scraping off the nanotubes from the Ti and Ti-Fe substrates. The unsupported pulverized flakes were placed in ceramic boats in a quartz tube furnace and annealed for 2 h at 450 °C in an ultrahigh-purity oxygen gas flow, at a heating/cooling rate of 1 °C/min. Results obtained from the nanotubes are compared with those measured from commercial TiO_2 (anatase) powder.

B. Characterization of TiO_2 nanotubes

Scanning electron microscopy (SEM, Hitachi S4800) was used to image the specimen morphology and SEM energy dispersive x-ray spectroscopy was employed to quantify an average Fe content in the nanotubes. The crystal structure of the nanotubes was probed using x-ray diffraction (XRD, Philips X'Pert Pro PANalytical) and the lattice parameters were calculated by a least-squares method and compared to the bulk anatase reference data [13].

Magnetic measurements were conducted using a superconducting quantum interference device magnetometer. The magnetization was measured as a function of temperature at $H_{\text{applied}} = 0.05\,\text{T}$ for $2\,\text{K} < T < 400\,\text{K}$, and as a function of magnetic field at $T = 2, 3, 6, 10$, and 300 K within the field range of $\mu_o H = \pm 5\,\text{T}$. The total magnetic susceptibility χ_{tot} of the nanotube samples was fit to the expression [14]:

$$\chi_{\text{tot}}(T) = C/(T - T_0) + \chi_{PP}, \tag{1}$$

where C is the Curie-Weiss constant that is related to the magnitude of the atomic magnetic moment, T_0 is the Curie-Weiss temperature that characterizes ferro- or antiferromagnetic interactions, and χ_{PP} is the Pauli paramagnetic susceptibility originating from electron occupancy at the Fermi energy. The average effective moment per Fe ion, $\langle \mu_{\text{eff}} \rangle_{Fe}$, was calculated from the Curie-Weiss constant using the expression [15,16]:

$$\mu_{\text{eff}} = \sqrt{3Ck_B/N}, \tag{2}$$

in which N is the number of Fe atoms per mole and k_B is the Boltzmann constant. The Pauli paramagnetism contribution to the total magnetic susceptibility was correlated with the density of states (DOS) at the Fermi level of the TiO_2 nanotubes, through the relationship [17]

$$\text{DOS}(E_f) = \chi_{PP}/2\mu_B^2. \tag{3}$$

The oxidation state of the Fe ions in the nanotubes was calculated by fitting the angular momentum quantum number, J, to the Brillouin function:

$$B_J(x) = \frac{2J+1}{2J}\text{ctnh}\left(\frac{(2J+1)x}{2J}\right) - \frac{1}{2J}\text{ctnh}\left(\frac{x}{2J}\right),$$
$$x \equiv gJ\mu_B H/k_B(T - T_0) \tag{4}$$

where g is the Landé g factor and H is the magnetic field [15].

Information regarding the element-specific electronic structure present at the nanotubes' surface describing the unoccupied states above the Fermi level was obtained using near-edge x-ray absorption fine structure spectroscopy (NEXAFS) [18,19]. These measurements were carried out at the U7A beamline of the National Synchrotron Light Source at Brookhaven National Laboratory.

The NEXAFS spectra were collected in the partial electron yield detection mode at room temperature under a vacuum better than 10^{-8} Torr, with the photon beam normal to the sample surface. Partial electron yield mode collects Auger electrons resulting in a probing depth of 2–4 nm, which makes NEXAFS a highly surface-sensitive technique. Data were acquired for the titanium $L_{3,2}$-edge, oxygen K-edge and the Fe $L_{3,2}$-edge, normalized to the incident photon flux and using a monochromator grating with an energy resolution of 0.2 eV. The x-ray absorption spectra of commercial reference metallic and oxide compounds [titanium foil (99.97%), Fe foil (99.5%), anatase (99.9%), rutile (99.99%), TiO (99.5%), Ti_2O_3 (99.8%), Fe_3O_4 (99.997%), Fe_2O_3 (99.99%), $FeTiO_3$ (99.8%), and Fe_2TiO_5 (99.9%) powder] were also examined for comparison. The reference compounds in foil or powder form, and the nanotubes in the form of finely pulverized free-standing flakes, were manually pressed into copper tape sample holders with a 1-mm depth and approximately 25-mm diameter and were charge-neutralized using a low-energy electron gun. The spectra were normalized to the intensity tail at energies larger than those of the O K-edge (550 eV), the Ti L-edge (485 eV), and the Fe L-edge (735 eV). Any possible shift in the collected spectra was noticed and corrected for, by referring to the main peak position of a reference mesh in the U7A beamline for each set of data. Deconvolution of the Ti $L_{3,2}$-edge spectra into individual peaks was carried out by fitting the spectra to six [seven] Voigt peaks in the as-synthesized [annealed] state, after subtracting two step functions simulating the $L_{3,2}$-edge jumps. The center of each peak was considered to be the absorption peak position, and the reported intensity of each absorption peak was assigned as the area under the peak.

III. RESULTS

The morphology, composition, crystal structure, magnetic properties, and electronic structure of the pure and the Fe-incorporated TiO_2 nanotubes were studied in the as-synthesized state and after annealing in oxygen. The relative cationic concentration of Fe, expressed as [Fe]/([Fe]+[Ti]), in the Fe-incorporated TiO_2 nanotubes was determined to be 2.1 ± 0.3 at. % and the main conclusions obtained are summarized as follows:

(1) Upon annealing at 450 °C in flowing oxygen the degree of crystallinity in the anatase phase was higher with Fe incorporation at both the surface and in the bulk of the nanotubes; the unit cell in the Ti-incorporated lattice is expanded relative to that of the pure (Fe-free) lattice.

(2) Titanium exists predominantly in the Ti^{4+} form in the pure TiO_2 nanotubes in both the as-synthesized and the annealed states. The Ti^{4+} concentration [i.e., $Ti^{4+}/(Ti^{3+} + Ti^{4+})$ ratio], however, was higher in Fe-incorporated nanotubes than in the pure nanotubes.

(3) The electronic density of states at the Fermi level of TiO_2 was larger in presence of Fe, as compared to that determined for Fe-free nanotubes.

(4) Fe was largely in the Fe^{3+} oxidation state in the annealed nanotube samples. Due to interfering presence of the

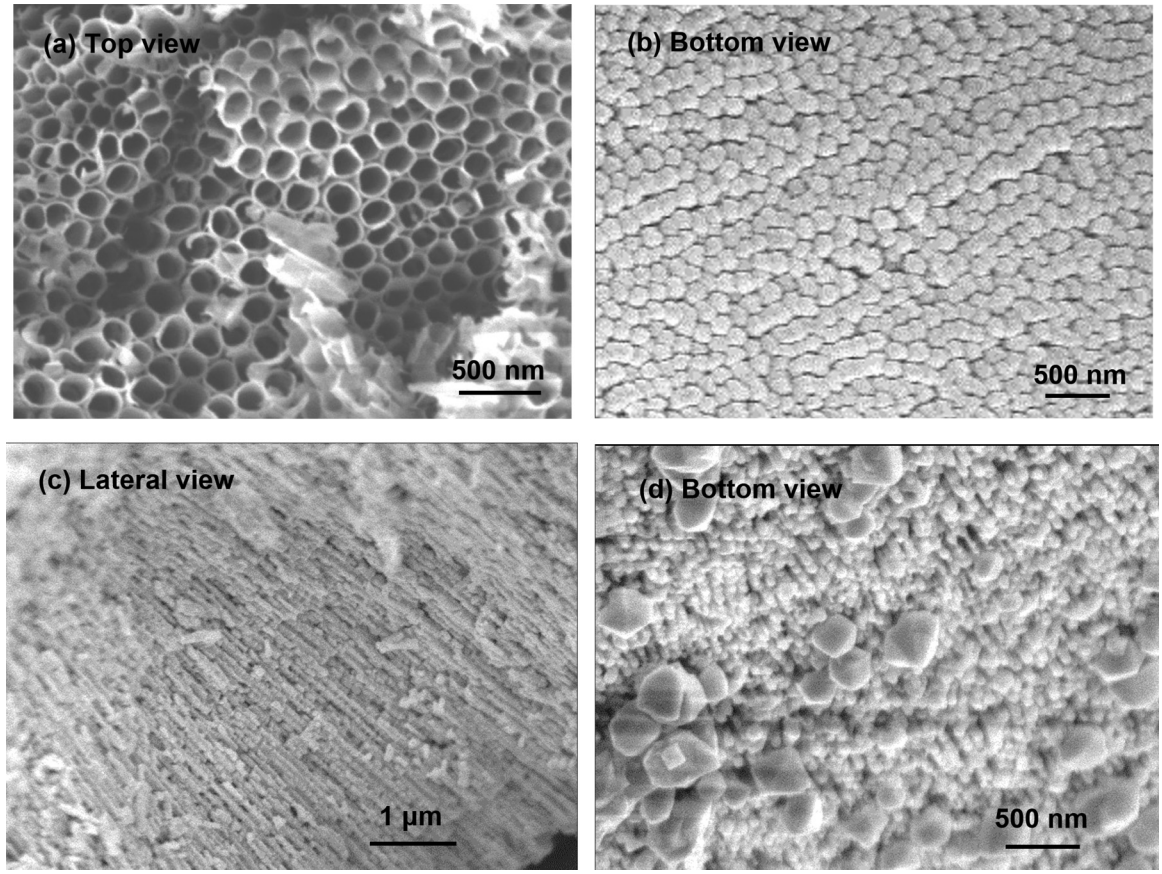

FIG. 1. Scanning electron microscopy images of the Fe-incorporated nanotubes in the (a), (b) as-synthesized state; and (c), (d) annealed in oxygen at 450 °C. The crystallites are formed in the nanotube scaffold.

fluorine (electrolyte residue remaining after electrochemical anodization) *K*-edge in the sample data, information on the oxidation state of Fe in the unannealed state was not extracted.

Details of these results are presented and discussed in the following sections.

A. Morphology, composition and crystal structure

In the as-synthesized state, the Fe-incorporated TiO_2 nanotubes feature an average length of ∼50 μm and a pore size of approximately 100 nm, very similar to the length and pore size of pure TiO_2 as-synthesized nanotubes. Upon annealing in oxygen at 450 °C, equiaxed nanoparticles (up to 250 nm) form on top of the pure and the Fe-incorporated nanotubes and the nanotube wall becomes fragmented to form a connected porous architecture [20,21]. Scanning electron microscope images of the nanotube arrays are shown in Figs. 1(a)–1(d).

Upon annealing, the amorphous as-synthesized nanotubes crystallize to form the anatase structure (tetragonal symmetry, space group $I4_1/amd$). The *a*- and *c*-lattice parameters of the Fe-incorporated nanotubes, calculated from the XRD data and plotted in Fig. 2(a), are slightly larger than those of the pure nanotubes, resulting in a subtle but definite volume expansion of the anatase unit cell, Fig. 2(b).

B. Magnetic characterization

The temperature dependencies of the magnetic susceptibility of the Fe-incorporated and the pure nanotubes in

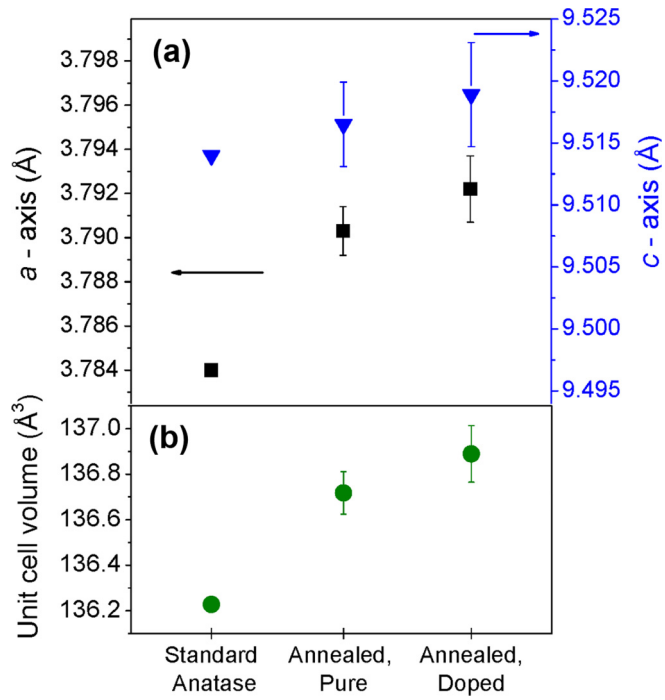

FIG. 2. (a) Lattice parameters and (b) unit cell volume of O_2-annealed pure and Fe-incorporated TiO_2 nanotubes showing an expansion of the crystal structure with Fe incorporation.

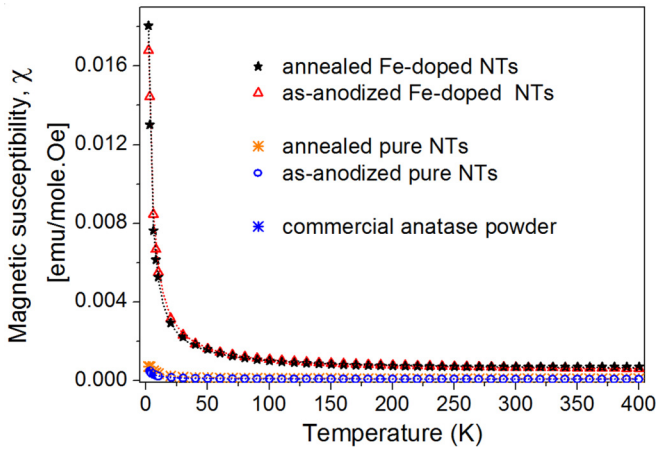

FIG. 3. Magnetic susceptibility of pure and Fe-incorporated TiO_2 nanotubes (NTs) measured at $H = 500$ Oe. Note that the low-temperature susceptibility is several orders of magnitude larger for Fe-incorporated samples, in comparison with the pure nanotubes and commercial anatase nanoparticles. The dotted curves are the fits to Eq. (1).

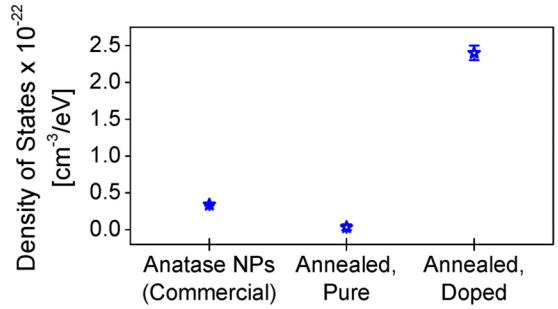

FIG. 4. Density of states (DOS) at the Fermi energy derived from the Pauli paramagnetic contribution of the moment, χ_{PP}, Eq. (3). The DOS for the Fe-incorporated sample is an order of magnitude larger than those of the commercial nanoparticles and the pure nanotubes.

both the as-synthesized and annealed states are plotted in Fig. 3. Compared with the susceptibility response of the pure nanotubes, the Fe-incorporated nanotube samples exhibit significantly larger susceptibility values, especially for $T <$ 100 K. The total magnetic susceptibility of all the nanotube samples could be modeled as consisting of (i) a temperature-dependent Curie-Weiss paramagnetic contribution and (ii) a temperature-independent Pauli paramagnetic contribution, and thus could be successfully fit to Eq. (1). Results from fitting the data to Eq. (1) are summarized in Table I. The Curie-Weiss temperature was found to be always small and negative, $-T_0 \sim 1$ to 4 K, indicating weak antiferromagnetic coupling between the Fe ions in the structure. In the as-made state, incorporation of Fe causes an order-of-magnitude increase in the Curie-Weiss constant relative to that of the pure as-made TiO_2 nanotubes, from $C = 2$ to 60 emu · K/Oe · mole. Annealing the nanotubes in flowing oxygen resulted in only a minor decrease in C of the Fe-incorporated nanotubes. Assuming that all of the incorporated Fe (2.1 ± 0.3 at. % Fe) contributes to the paramagnetic moment, the corresponding effective moment per Fe atom is $\langle \mu_{\text{eff}} \rangle_{Fe} = 4.8 \pm 0.9\, \mu_B$/Fe in the as-synthesized nanotubes and $4.4 \pm 0.9\, \mu_B$/Fe in the annealed Fe-incorporated nanotubes, where μ_B is the Bohr magneton. These values for the effective moments assume that all of the Fe ions contribute equally, which results in a relatively large 20% uncertainty in the effective moments.

The Pauli paramagnetic contribution to the moment was found to be larger for the Fe-incorporated nanotubes as compared to that of the pure nanotubes. Also, annealing the as-synthesized Fe-incorporated nanotubes in oxygen increases the value of χ_{PP} by approximately 20%. Quantification of χ_{PP} allows computation and comparison of values of the DOS at the Fermi level for Fe-incorporated and pure TiO_2 nanotubes, as described in Eq. (3). Figure 4 shows that Fe incorporation increases the nanotube DOS at the Fermi level by an order of magnitude. It is important to note that the DOS is a critical factor in determination of the catalytic properties [22].

Assuming that the low-temperature magnetic moment of the nanotubes is dominated by the Fe cations, the ionic state of Fe in the lattice can be identified by determining the angular momentum quantum number, J, using the Brillouin function as applied to thermomagnetization data, Eq. (4). The first test to verify Brillouin behavior is to ensure that the magnetic data scales appropriately with temperature. Figure 5(a) displays the magnetization of the nanotube samples, excluding their Pauli paramagnetic contribution, as a function of $H/(T - T_0)$ and demonstrates that the data overlap for three measurement temperatures $T = 3$, 6, and 10 K. A Brillouin function behavior is therefore confirmed, since the temperature scaling is satisfactory using $T_0 = -0.9$ K. It should be noted that a negative value of T_0 indicates that there is a small Fe-Fe exchange interaction that is predominantly antiferromagnetic. Figure 5(b) shows an excellent fit of the $T = 3$ K data to the

TABLE I. Magnetic properties of pure and Fe-incorporated TiO_2 nanotubes (NTs) in as-synthesized and oxygen-annealed samples, compared with those of commercial nanoparticles (NPs). The Curie-Weiss constant, C, and the temperature-independent Pauli paramagnetic contribution χ_{PP} to the total magnetic susceptibility is also included, based on fitting the magnetic susceptibility to Eq. (1), $\chi_{\text{tot}}(T) = C/(T - T_0) + \chi_{PP}$. Note the nearly 100 times increase in C and χ_{PP} for TiO_2 nanotubes with Fe incorporation.

TiO_2 Samples	$C \times 10^3$ [emu · K/Oe · mole]	$\chi_{PP} \times 10^6$ [emu/Oe·mole]	T_0 [K]
Pure NTs, as-synthesized	2.0 ± 0.1	6.2 ± 0.8	− 1.7 ± 0.1
Pure NTs, annealed	3.8 ± 0.2	7 ± 2	− 3.6 ± 0.2
Fe-incorporated NTs, as-synthesized	60.0 ± 1.0	440 ± 30	− 1.8 ± 0.1
Fe-incorporated NTs, annealed	50 ± 4	530 ± 10	− 0.9 ± 0.1
Commercial anatase nanoparticles	0.6 ± 0.1	74.0 ± 1.0	− 1.3 ± 0.2

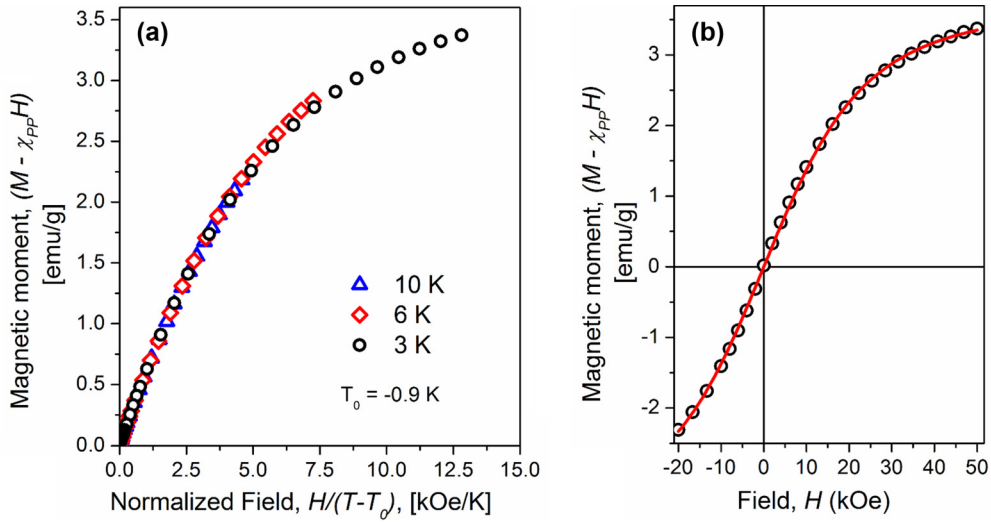

FIG. 5. (a) Magnetic moment of the annealed Fe-incorporated nanotubes as a function of the temperature-normalized field, $H/(T - T_0)$, confirming that the magnetic moment follows the modified Brillouin behavior. (b) Plot of the low-temperature ($T = 3$ K) magnetic moment of the annealed Fe-incorporated nanotubes fit to the modified Brillouin function Eq. (4) yielding $J = 5/2$, corresponding to nearly isolated Fe^{3+} ions.

Brillouin function using $J = 5/2$. The same $J = 5/2$ value was also obtained from analysis of the M-T data obtained from the as-synthesized Fe-incorporated nanotubes (data not shown here). A value of $J = 5/2$ corresponds to Fe^{3+} cations, assuming a sole contribution from the spin moment due to quenching of the orbital moment [23,24].

C. Electronic structure and local environment

Changes in the electronic structure of titanium, iron, and oxygen are produced via Fe incorporation and by annealing; these changes are examined by comparing the element-specific NEXAFS data of the nanotube samples with data obtained from reference compounds. In the following sections, x-ray absorption spectra of the O *K*-edge, and Ti and Fe $L_{3,2}$-edges in pure and Fe-incorporated nanotubes and in the reference compounds are studied in detail.

Oxygen K-edge NEXAFS: The NEXAFS spectra at O *K*-edge in pure and in Fe-incorporated nanotubes consist of two prominent features in the energy range of 527–550 eV, Fig. 5. The first set of peaks (527–535 eV) represents the transition of O-*1s* electrons to the O-$2p_\pi$ and O-$2p_\sigma$ states hybridized with Ti *3d* bands that are classified as subgroups t_{2g} and e_g, respectively. The higher-energy set of peaks (535–550 eV) originates from the delocalization of the antibonding states of the O-*2p* and Ti-*4sp* electrons [25–28]. The absorption peaks of both pure and Fe-incorporated nanotubes are broad in the as-synthesized state; after annealing, however, the first set of peaks becomes sharper and new features appear. Comparison of the O *K*-edge peak features of the annealed nanotubes with those of the reference Ti- and Fe-based oxide compounds, Fig. 6, indicates that the anatase structure forms in the nanotubes upon annealing, consistent with the results of the XRD measurements. No significant change in the electronic structure of the oxygen component in TiO_2 was observed in the presence of Fe, as attested to by the similar peak positions of the O *K*-edge in both pure and Fe-incorporated nanotubes.

Ti$L_{3,2}$-edge NEXAFS: The NEXAFS at Ti $L_{3,2}$-edge can reveal the elemental local structure in TiO_2 [26,29]. Within the energy range of 455–470 eV, two main doublet peaks corresponding to the L_3 and L_2 edges are observed in the absorption spectra of the nanotubes and oxide compounds, Fig. 7(a). The Ti $L_{3,2}$-edge features arise from Ti $2p^6 \rightarrow$

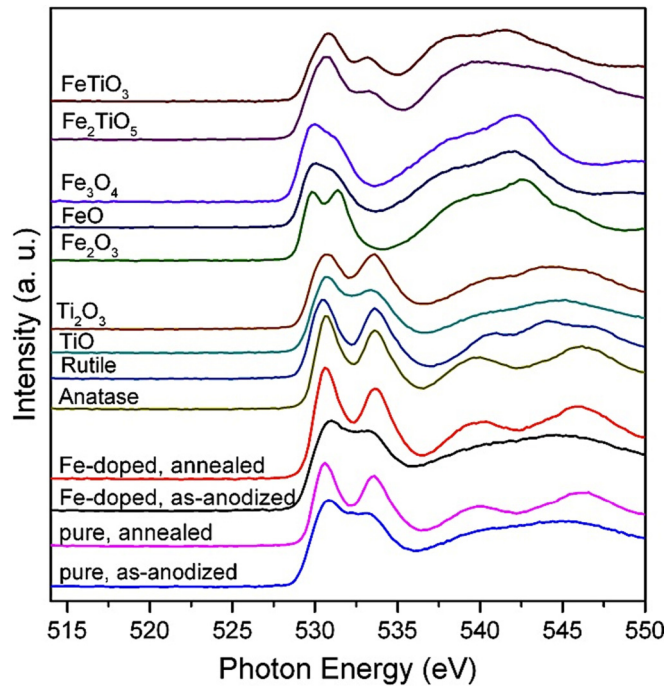

FIG. 6. The O *K*-edge NEXAFS spectra of pure and Fe-incorporated TiO_2 nanotubes in the as-synthesized and annealed states, compared to those of the oxide reference compounds, showing a negligible difference in the peak features of pure nanotubes upon Fe incorporation.

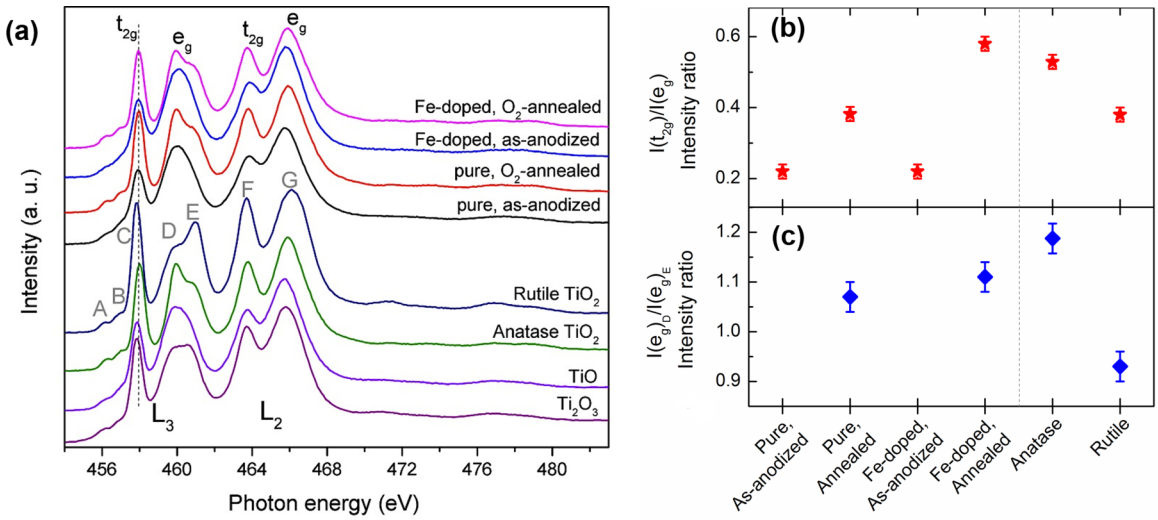

FIG. 7. Normalized Ti $L_{3,2}$-edge NEXAFS spectra for the pure and Fe-incorporated TiO_2 nanotubes in the as-synthesized and annealed states, as compared to those of the reference compounds. (b), (c) Intensity ratio of the Ti L_3-edge features for the as-synthesized and annealed Fe-incorporated TiO_2 nanotubes, compared to the anatase and rutile structures, (b) $I(L_3\text{-}t_{2g})/I(L_3\text{-}e_g)$ and (c) $I(e_g)_D/I(e_g)_E$ intensity ratios.

$2p^5 3d^1$ transitions (i.e., from the Ti $2p$ core level to the unoccupied $3d$ energy state) [27,30,31]. The strength of the crystal field causes the doublet features for each edge to split into the t_{2g} and e_g subbands. The additional energy splitting of approximately 1 eV at the e_g level, peaks D and E in Fig. 7(a), is likely due to breaking the degeneracy between $d_{x^2-y^2}$ and d_{z^2} orbital sublevels and is attributed to the off-center displacement of Ti ions in different configurations [32]. It should be noted that no pronounced e_g splitting is observed in the as-synthesized nanotube samples of either composition. Absence of such splitting highlights the averaging effect of the amorphous structural state on the $3d$ sublevels. Upon annealing, a doublet feature in the L_3-e_g peak appears, Fig. 7(a), and is accompanied by a sharpening of the low-energy features (peaks A and B in the same figure) that resembles those of the anatase absorption spectrum.

Detailed analysis of the Ti $L_{3,2}$-edge peaks through examination of the peak intensity ratios, Figs. 7(b) and 7(c), reveals a sizeable variation in the $I(L_3\text{-}t_{2g})/I(L_3\text{-}e_g)$ intensity ratio, which indicates an analogous variation in the character of the unoccupied energy states [30]. Quantitative comparison of the intensities of peaks C and (D+E), i.e., the $I(L_3\text{-}t_{2g})/I(L_3\text{-}e_g)$ intensity ratio in Fig. 7(b), shows that the titanium $I(L_3\text{-}t_{2g})/I(L_3\text{-}e_g)$ intensity ratio measured for both pure and Fe-incorporated nanotubes increases upon annealing, which indicates an increase in the overall Ti^{4+} concentration. Furthermore, the intensity ratio of peaks D and E [corresponding to subband transitions at the Ti L_3-e_g orbital, as designated in Fig. 7(a)], can clarify the type of the crystal structure, with anatase [rutile] having an $I(e_g)_D/I(e_g)_E$ intensity ratio of larger [smaller] than 1 [33]. Both the pure and the Fe-incorporated nanotube samples have a Ti $I(e_g)_D/I(e_g)_E$ intensity ratio >1, Fig. 7(c), confirming the dominance of the anatase structure in the probed population of nanotubes. This intensity ratio determined for the annealed Fe-incorporated nanotubes is slightly larger than that of the annealed pure nanotubes, confirming the slightly higher anatase content in the Fe-incorporated nanotubes.

Fe $L_{3,2}$-edge NEXAFS: The Fe $L_{3,2}$-edge is reported to be very sensitive to the Fe oxidation state [31,34]. The absorption spectra of the Fe $L_{3,2}$-edge for the Fe-incorporated nanotubes in the as-synthesized and annealed states are shown in Fig. 8(a), compared to those of the reference Fe-based compounds. The Fe L-edge spectra are separated into the L_3 and L_2 edges by spin-orbit coupling in the core levels; these L_3 and L_2 edges correspond to transitions from the $2p_{3/2}$ and $2p_{1/2}$ core levels, respectively, to the unoccupied $3d$ states in the valence band [35]. Additional spectral features within the L_3 or L_2 envelope arise from contributions from different Fe cation valence states as well as from variations in the overlap integral of the photoexcited electron and the core-hole produced in the resonant x-ray absorption process [35–38]. The fluorine (F) K-edge (680–705 eV) is also observed in the absorption spectra of the as-synthesized Fe-incorporated nanotubes and is a result of the residual fluorine from the electrochemical anodization synthesis process. Fluorine is substantially removed during the course of annealing [39], as confirmed by the disappearance of the F K-edge, Fig. 8(a).

Extraction of detailed qualitative information from the Fe $L_{3,2}$-edge absorption spectrum of the as-synthesized Fe-incorporated nanotubes is challenging for three reasons: (1) the presence of significant amounts of fluorine in the as-synthesized nanotubes and the overlap of the F K-edge with the Fe $L_{3,2}$-edge, (2) the small amount of Fe in the nanotubes, and (3) the instability of the electronic structure of Fe in the as-synthesized nanotubes during the NEXAFS measurements when they were exposed to the x-ray scans in vacuum, as shown in Fig. 8(b). The Fe L_3-edge peak of the as-synthesized nanotubes clearly shows a split feature designated as peaks α and β in Fig. 8(b). The intensity of peak α is larger than that of the peak β in the Fe^{2+}-containing oxide species, where peak β appears as a weak shoulder. In Fe^{3+}-containing oxide species, however, this intensity ratio is reversed [36]. In the first x-ray scan, the peak intensity ratio $\alpha/\beta < 1$, but when the nanotubes undergo further x-ray scans, the intensity of

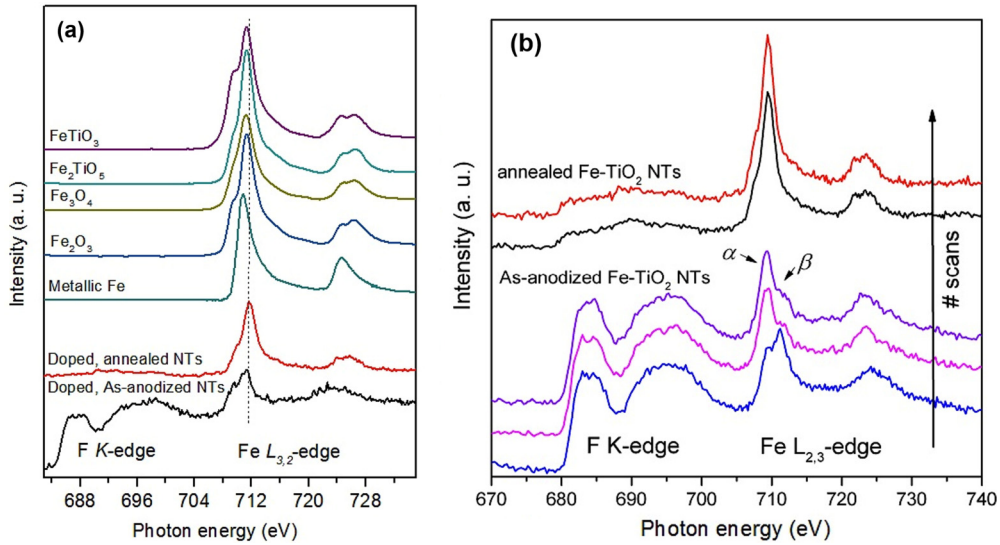

FIG. 8. (a) NEXAFS spectra at Fe $L_{3,2}$-edge for the as-synthesized and annealed Fe-incorporated TiO_2 nanotubes, as compared to that of the metallic Fe confirming a higher oxidation state of Fe in the nanotubes. (b) NEXAFS spectra at the Fe $L_{3,2}$-edge collected for the sequential synchrotron x-ray scans on the as-synthesized and annealed Fe-incorporated TiO_2 nanotubes.

peak α increases while that of the peak β diminishes. This change in the intensity of the L_3-edge peak split features indicates a photochemical change in the Fe electronic structure upon irradiation with x-rays in vacuum. In the oxygen-annealed nanotubes, however, no change in the shape of L_3 peak is observed with increased number of x-ray scans, and the α/β intensity ratio is much smaller than that of the as-synthesized nanotubes, consistent with a more stable electronic structure of Fe^{3+}.

IV. DISCUSSION

The subtle expansion observed in the lattice structure of the crystalline Fe-incorporated nanotubes in comparison with that of the pure nanotubes can be attributed to the Fe ions substituting for some of the Ti ions in the anatase crystal structure. Even though the Fe^{3+} cationic radius is smaller than that of Ti^{4+} (0.55 Å versus 0.61 Å for coordination number of 6 [40]), this substitution can expand the lattice by virtue of weakened bonding alterations and the possible formation and stabilization of structural defects such as oxygen vacancies [20,41], which form to maintain the charge neutrality [42]. Both the magnetic characterization and the x-ray absorption spectroscopy results suggest the dominance of Fe ions in the Fe^{3+} oxidation state. Atomic magnetic moments estimated for the as-synthesized and annealed Fe-containing nanotube samples were $\langle \mu_{\text{eff}} \rangle_{Fe} = 4.8$ and $4.4\,\mu_B$/Fe, respectively, in full agreement with a total angular momentum of $\boldsymbol{J} = 5/2$ from Fe^{3+} cations. A deviation from the reported value of $\langle \mu_{\text{eff}} \rangle_{Fe} = 5.92\,\mu_B/Fe^{3+}$ [43] can indicate some degree of electron itinerancy, likely due to the presence of oxygen vacancies [20,44]. It has been reported that the presence of the antisite Fe^{3+} ions causes formation of a new energy band in the TiO_2 band gap, and the mixing of the Ti and Fe d orbitals can decrease the band gap energy between the Ti-d band and O-p band of the TiO_2 structure [45]. On the other hand, the shape of the Fe L_3-edge absorption spectrum for the annealed nanotube sample indicates the dominance Fe^{3+} ions rather than Fe^{2+} [36]. Thus, it is concluded that iron in the annealed Fe-incorporated nanotubes is mostly present in the form of Fe^{3+}. Annealing the nanotubes promotes a slight decrease in the effective magnetic moment, accompanied by a subtle increase in the Pauli paramagnetic contribution of the total magnetic susceptibility, and thus it may be concluded that the density of states at the Fermi level increases upon annealing. The x-ray absorption spectroscopy data indicate an increase in the oxidation state of Fe upon annealing, transitioning from a Fe^{2+}-dominant state to a Fe^{3+}-dominant state. Finally, the change in the electronic structure of Fe in the as-synthesized nanotubes from a Fe^{3+}-dominant to a Fe^{2+}-dominant state from sequential x-ray irradiations during the course of the experiments may be explained by photochemistry-induced changes of the nanotubes, and perhaps an x-ray-induced reduction of Fe^{3+} to Fe^{2+} [46].

V. CONCLUSIONS

In summary, amorphous Fe-incorporated TiO_2 nanotubes were fabricated by anodization of arc-melted Ti-Fe foil. The anatase crystal structure was obtained after annealing in an oxygen-containing environment. The oxidation state of iron in the annealed Fe-modified TiO_2 nanotubes was predominantly in the form of Fe^{3+}, which most likely substitutes for the Ti^{4+} ions in the anatase lattice and contributes to formation/stabilization of oxygen vacancies. The effect of Fe-incorporation in the anatase structure was observed as an expanded anatase unit cell volume, increased localized magnetic moment and higher density of states at the Fermi level. These changes in the crystal structure, magnetic behavior and electronic structure of TiO_2 nanotubes may be associated with alterations in the functionality of TiO_2 nanotubes for energy-related applications.

ACKNOWLEDGMENTS

This paper is based upon work supported by the National Science Foundation (Grants No. DMR-0906608, No. DMR-0907007, and No. ECCS-1402738). Use of the National Synchrotron Light Source, Brookhaven National Laboratory, was supported by the US Department of Energy, Office of Basic Energy Sciences (Contract No. DE-AC02-98CH10886).

[1] Y. Matsumoto, M. Murakami, T. Shono, T. Hasegawa, T. Fukumura, M. Kawasaki, P. Ahmet, T. Chikyow, S. Koshihara, and H. Koinuma, Room-temperature ferromagnetism in transparent transition metal-doped titanium dioxide, Science **291**, 854 (2001).

[2] J. M. Macak, H. Tsuchiya, A. Ghicov, K. Yasuda, R. Hahn, S. Bauer, and P. Schmuki, TiO_2 nanotubes: Self-organized electrochemical formation, properties and applications, Curr. Opin. Solid State Mater. Sci. **11**, 3 (2007).

[3] C. Richter, C. Jaye, E. Panaitescu, D. A. Fischer, L. H. Lewis, R. J. Willey, and L. Menon, Effect of potassium adsorption on the photochemical properties of titania nanotube arrays, J. Mater. Chem. **19**, 2963 (2009).

[4] I. Paramasivam, H. Jha, N. Liu, and P. Schmuki, A Review of photocatalysis using self-organized TiO_2 nanotubes and other ordered oxide nanostructures, Small **8**, 3073 (2012).

[5] K. Shankar, J. I. Basham, N. K. Allam, O. K. Varghese, G. K. Mor, X. Feng, M. Paulose, J. A. Seabold, K.-S. Choi, and C. A. Grimes, Recent advances in the use of TiO_2 nanotube and nanowire arrays for oxidative photoelectrochemistry, J. Phys. Chem. C **113**, 6327 (2009).

[6] S. M. Bedair, J. M. Zavada, and N. El-Masry, A spin to remember, IEEE Spectrum **47**, 44 (2010).

[7] S. A. Wolf, D. D. Awschalom, R. A. Buhrman, J. M. Daughton, S. von Molnar, M. L. Roukes, A. Y. Chtchelkanova, and D. M. Treger, Spintronics: A spin-based electronics vision for the future, Science **294**, 1488 (2001).

[8] L. Guangzhong, Z. Wenyan, Z. Jian, L. Yaning, K. Xinting, and T. Huiping, A novel way to fabricate Fe doped TiO_2 Nanotubes by Anodization of TiFe Alloys, Rare Metal Mat. Eng. **40**, 1510 (2011).

[9] X. Wang, J. Zhao, Y. Kang, L. Li, and X. Xu, Photoelectrochemical properties of Fe-doped TiO_2 nanotube arrays fabricated by anodization, J. Appl. Electrochem. **44**, 1 (2014).

[10] M. Guo, J. Zhao, X. Xu, G. Liu, and X. Wang, Preparation and magnetic properties of iron titanium oxide nanotube arrays, Ceram. Int. **40**, 5825 (2014).

[11] S. A. Ahmed, Ferromagnetism in Cr-, Fe-, and Ni-doped TiO_2 samples, J. Magn. Magn. Mater. **442**, 152 (2017).

[12] Qingyao Wang, Rencheng Jin, Miao Zhang, and Shanmin Gao, Solvothermal preparation of Fe-doped TiO_2 nanotube arrays for enhancement in visible light induced photoelectrochemical performance. Alloys Compd. **690**, 139 (2017).

[13] PDF#71-1166, M. D. Jade Software, 5.30.37 Materials Data Inc.

[14] F. E. Senftle, T. Pankey, and F. A. Grant, Magnetic susceptibility of tetragonal titanium dioxide, Phys. Rev. **120**, 820 (1960).

[15] J. B. Goodenough, *Magnetism and the Chemical Bond* (Interscience Publishers, New York, 1963), pp. 13–17.

[16] C. Kittel, *Introduction to Solid State Physics* (John Wiley & Sons, Inc., New York, 1968), pp. 432–435.

[17] L. H. Lewis, E. Baumberger, and R. J. Gambino, Magnetic ordering in Pd/Mn oxide nanocomposites, J. Appl. Phys. **99**, 08P901 (2006).

[18] F. M. de Groot, J. C. Fuggle, B. T. Thole, and G. A. Sawatzky, $L_{2,3}$x-ray-absorption edges of D_0 compounds: K^+, Ca^{2+}, Sc^{3+}, and Ti^{4+} in O_h (Octahedral) symmetry, Phys. Rev. B **41**, 928 (1990).

[19] C. L. Chen, C. L. Dong, K. Asokan, J. L. Chen, Y. S. Liu, J.-H. Guo, W. L. Yang, Y. Y. Chen, F. C. Hsu, C. L. Chang, and M. K. Wu, Role of 3d electrons in the rapid suppression of superconductivity in the dilute V-doped spinel superconductor $LiTi_2O_4$, Supercond. Sci. Technol. **24**, 115007 (2011).

[20] P. M. Hosseinpour, E. Panaitescu, D. Heiman, L. Menon, and L. H. Lewis, Toward tailored functionality of titania nanotube arrays: Interpretation of the magnetic-structural correlations, J. Mater. Res. **28**, 1304 (2013).

[21] P. M. Hosseinpour, E. Panaitescu, J. Lim, J. Morris, L. H. Lewis, and L. Menon, Morphology and structure of heat-treated titania nanotubes, Nanomater. Energy **2**, 35 (2013).

[22] D. A. Stewart and F. Leonard, Photocurrents in Nanotube Junctions, Phys. Rev. Lett. **93**, 107401 (2004).

[23] J. L. G. A. Marshall Stoneham, *Dynamics at the Nanoscale in Handbook of Nanophysics, Principles and Methods* (CRC Press, Boca Raton, FL, 2011), p. 13.

[24] B. Henderson and G. V. Raynor, The paramagnetic susceptibility of face-centred cubic silver-manganese and silver-tin-manganese alloys, J. Phys. Radium **23**, 685 (1962).

[25] G. Vanderlaan, Polaronic satellites in x-ray-absorption spectra, Phys. Rev. B **41**, 12366 (1990).

[26] R. Ruus, A. Kikas, A. Saar, A. Ausmees, E. Nommiste, J. Aarik, A. Aidla, T. Uustare, and I. Martinson, Ti-2p and O-1s X-ray absorption of TiO_2 Polymorphs, Solid State Commun. **104**, 199 (1997).

[27] S. Kumar, Alimuddin, R. Kumar, P. Thakur, K. H. Chae, B. Angadi, and W. Choi, Electrical transport, magnetic, and electronic structure studies of $Mg_{(0.95)}Mn(0.05)Fe_{(2-2x)}Ti_{2x}O_{4\pm\delta}$($0 \leqslant X \leqslant 0.5$) ferrites, J. Phys.: Condens. Matter **19**, 476210 (2007).

[28] S. J. Chen, J. S. Garitaonandia, D. Ortega, and K. Suzuki, Room-temperature spontaneous magnetization in a nanostructured TiO_2-Al system prepared by ball-milling, J. Alloys Compd. **536**, S287 (2012).

[29] J. G. Chen, NEXAFS Investigations of transition metal oxides, nitrides, carbides, sulfides and other interstitial compounds, Surf. Sci. Rep. **30**, 1 (1997).

[30] L. Soriano, M. Abbate, J. Vogel, J. C. Fuggle, A. Fernandez, A. R. Gonzalezelipe, M. Sacchi, and J. M. Sanz, Chemical-changes induced by sputtering in TiO_2 and some selected titanates as observed by x-ray-absorption spectroscopy, Surf. Sci. **290**, 427 (1993).

[31] D. K. Shukla, S. Mollah, R. Kumar, P. Thakur, K. H. Chae, W. K. Choi, and A. Banerjee, Effect of Ti substitution on

multiferroic properties of $BiMn_2O_5$, J. Appl. Phys. **104**, 033707 (2008).

[32] C. Schmitz-Antoniak, D. Schmitz, P. Borisov, F. M. F. de Groot, S. Stienen, A. Warland, B. Krumme, R. Feyerherm, E. Dudzik, W. Kleemann, and H. Wende, Electric in-plane polarization in Multiferroic $CoFe_2O_4/BaTiO_3$ nanocomposite tuned by magnetic fields, Nat. Commun. **4**, 2051 (2013).

[33] M. Y. Hsu, W. C. Yang, H. Teng, and J. Leu, Microstructure and composition of TiO_2 nanotube arrays fabricated with HF and NH_4F electrolytes and their evolution during annealing, J. Electrochem. Soc. **158**, K81 (2011).

[34] B. Gilbert, J. E. Katz, J. D. Denlinger, Y. D. Yin, R. Falcone, and G. A. Waychunas, Soft x-ray spectroscopy study of the electronic structure of oxidized and partially oxidized magnetite nanoparticles, J. Phys. Chem. C **114**, 21994 (2010).

[35] J. Leveneur, G. I. N. Waterhouse, J. Kennedy, J. B. Metson, and D. R. G. Mitchell, Nucleation and growth of Fe Nanoparticles in SiO_2: A TEM, XPS, and Fe L-Edge XANES investigation, J. Phys. Chem. C **115**, 20978 (2011).

[36] F. Jiménez-Villacorta, C. Prieto, Y. Huttel, N. D. Telling, and G. van der Laan, X-ray magnetic circular dichroism study of the blocking process in nanostructured iron-iron oxide core-shell systems, Phys. Rev. B **84**, 172404 (2011).

[37] R. K. Hocking and E. I. Solomon, *Ligand Field and Molecular Orbital Theories of Transition Metal X-ray Absorption Edge Transitions in Molecular Electronic Structures of Transition Metal Complexes I* (Springer-Verlag, Berlin, 2012).

[38] J. R. Hayes and A. P. Grosvenor, An x-ray absorption spectroscopic study of the electronic structure and bonding of rare-earth orthoferrites, J. Phys. Condens. Matter **23**, 465502, (2011).

[39] J. M. Macak, S. Aldabergerova, A. Ghicov, and P. Schmuki, Smooth anodic TiO_2 nanotubes: Annealing and structure, Phys Status Solidi A **203**, R67 (2006).

[40] D. R. Lide, *CRC Handbook of Physics and Chemistry* (CRC Press, Boca Raton, Florida, 2010), p. 4–147.

[41] C. Adan, A. Bahamonde, M. Fernandez-Garcia, and A. Martinez-Arias, Structure and activity of nanosized iron-doped anatase TiO_2 catalysts for phenol photocatalytic degradation, Appl. Catal., B **72**, 11 (2007).

[42] D. H. Hanaor and C. Sorrell, Review of the anatase to rutile phase transformation, J. Mater. Sci. **46**, 855 (2011).

[43] C. E. Rodríguez-Torres, A. F. Cabrera, L. A. Errico, C. Adán, F. G. Requejo, M. Weissmann, and S. J. Stewart, Local structure and magnetic behaviour of Fe-doped TiO_2 anatase nanoparticles: Experiments and calculations, J. Phys. Condens. Matter **20**, 135210 (2008).

[44] Li-Ting Tseng, Xi Luo, Nina Bao, Jun Ding, Sean Li, and Jiabao Yi, Structures and properties of transition-metal-doped TiO_2 nanorods, Mater. Lett. **170**, 142 (2016).

[45] G. K. Mor, H. E. Prakasam, O. K. Varghese, K. Shankar, and C. A. Grimes, Vertically oriented Ti-Fe-O nanotube array films: Toward a useful material architecture for solar spectrum water photoelectrolysis, Nano Lett. **7**, 2356 (2007).

[46] M. Seki, A. K. M. Akther Hossain, T. Kawai, and H. Tabata, High-temperature cluster glass state and photomagnetism in Zn- and Ti-substituted $NiFe_2O_4$ films, J. Appl. Phys. **97**, 083541 (2005).